View Article Online / Journal Homepage / Table of Contents for this issue
Dynamic Article Links

PCCP

Cite this: *Phys. Chem. Chem. Phys.*, 2011, **13**, 4715–4723

www.rsc.org/pccp

PAPER

Published on 31 January 2011. Downloaded by Dalian Institute of Chemical Physics, CAS on 9/2/2019 6:21:22 AM.

Visible emission characteristics from different defects of ZnS nanocrystals

Xiuli Wang,[ab] Jianying Shi,[a] Zhaochi Feng,[a] Mingrun Li[a] and Can Li*[a]

Received 27th August 2010, Accepted 22nd December 2010
DOI: 10.1039/c0cp01620a

Various sized ZnS nanocrystals were prepared by treatment under H_2S atmosphere. Resonance Raman spectra indicate that the electron–phonon coupling increases with increasing the size of ZnS. Surface and interfacial defects are formed during the treatment processes. Blue, green and orange emissions are observed for these ZnS. The blue emission (430 nm) from ZnS without treatment is attributed to surface states. ZnS sintered at 873 K displays orange luminescence (620 nm) while ZnS treated at 1173 K shows green emission (515 nm). The green luminescence is assigned to the electron transfer from sulfur vacancies to interstitial sulfur states, and the orange emission is caused by the recombination between interstitial zinc states and zinc vacancies. The lifetimes of the orange emission are much slower than that of the green luminescence and sensitively dependent on the treatment temperature. Controlling defect formation makes ZnS a potential material for photoelectrical applications.

1. Introduction

Tailoring the color output of nanomaterials is very important for their applications as light emitting displays, field emitters,[1,2] lasers, sensors[3] and optoelectronic devices to multiplexed biological labeling.[4–7] Zinc sulfide (ZnS) is a suitable semiconductor as a host matrix for a wide variety of dopants on account of its wide energy band gap. The luminescence properties of ZnS particles have been tuned by doping with various transition metals and rare-earth metals.[8–11] For example, $ZnS:Cu^{2+}$, $ZnS:Eu^{2+}$, and $ZnS:Mn^{2+}$ nanocrystals show blue (460 nm), green (518 nm) and orange emission (590 nm), respectively.[12]

With the fast development of nanotechnology, ZnS unique nanostructures, such as nanowires, nanobelts and nanotubes, have been successfully synthesized.[13] ZnS nanostructures exhibit various optical properties, because the optical properties are sensitive to size, shape, crystal structure, and defects.[14] A near-UV emission band at about 400 nm is observed from ZnS nanowires,[15] nanobelts,[16] nanoribbons,[15,17] and multiangular branched nanostructures.[18] ZnS nanobelts[16] and nanoribbons[17] exhibit a blue emission band around 450 nm. Moreover, ZnS nanobelts,[19–21] nanotubes[22] and nanoribbons[17,23,24] can show a green emission centered at about 520 nm. More interestingly, the novel hierarchical ZnS/SiO_2 nanowires heterostructures show a strong orange emission at about 558 nm and a weak emission at about 720 nm,[25] and the ZnS nanotowers display two strong emission bands located at 394 nm and 592 nm.[26] In summary, various emission features, including the near-UV, blue, green and orange emission bands, have been observed for ZnS with nanostructures. These researches show the possibility of tuning various emission characteristics from pure ZnS nanocrystals with different defect properties.

The origins of the various photoluminescence (PL) bands from ZnS are rarely studied, though much effort has been made to investigate the optical features. The luminescence features of ZnS are commonly assigned to surface states,[27,28] sulfur vacancies,[29,30] zinc vacancies,[31–34] elemental sulfur species[20,35] or impurities[17,36] in ZnS. However, it is still unclear what are the luminescent sites contributing to each of the luminescence bands.

In the present work, ZnS samples with blue, green or orange luminescence were successfully prepared just through post-treatment of ZnS nanoparticles in H_2S atmosphere. The origins of the various luminescence bands were studied with photoluminescence excitation (PLE) spectra and time-resolved photoluminescence spectra. Changes in energy levels and quantity of defect states were also discussed for ZnS samples during heat treatment processes.

2. Experimental methods

2.1 Sample preparation

ZnS nanoparticles were synthesized in water by dropwise addition of 0.05 M Na_2S to 0.05 M $Zn(CH_3COO)_2{\cdot}2H_2O$ at room temperature. After the white precipitate was stirred for 24 h, it was filtered and washed three times with deionized water and anhydrous ethanol, respectively. Finally, the sample

[a] *State Key Laboratory of Catalysis, Dalian Institute of Chemical Physics, Chinese Academy of Sciences, P. O. Box 110, Dalian 116023, China. E-mail: canli@dicp.ac.cn; Fax: +86-411-84694447; Tel: +86-411-84379070*
[b] *Graduate University of Chinese Academy of Sciences, Beijing 100049, China*

View Article Online

Published on 31 January 2011. Downloaded by Dalian Institute of Chemical Physics, CAS on 9/2/2019 6:21:22 AM.

was dried at 353 K in vacuum. The obtained sample was denoted as "ZnS-P". The ZnS-P was then sintered at high temperature ranging from 873 K to 1173 K for 2 h, and the obtained samples were denoted as "ZnS-T". During the whole treatment process, the tubular furnace was purged continuously with 5% H_2S gas in Ar.

ZnS films on quartz disk were prepared as follows in order to do PL measurements at cryogenic temperatures. 6 mg ZnS was suspended in 0.5 mL water and sonicated for 15 min. 200 μL of this suspension was dropped onto a 15-mm diameter quartz disk and dried slowly in air. A homogeneous film of ZnS on the quartz disk was obtained with this method. It is difficult to estimate the precise dependence of the PL efficiency on the ZnS structure because of the inhomogeneous distribution of the particle density in the film samples. However, we can discuss the photoexcited carrier dynamics from the PL spectral shapes and lifetimes.

2.2 Characterization methods

The steady-state and time-resolved PL spectra at cryogenic temperatures were carried out on a FLS920 fluorescence spectrometer (Edinburgh Instruments). A 450 W Xe lamp was used as the excitation source for the steady-state PL spectra, while a μF920 microsecond flash lamp with a pulse width of ~2 μs was the excitation light for the time-resolved PL measurements. Low-temperature experiments of ZnS samples were carried out inside a variable temperature Oxford cryostat model OptistatDN (77 to 500 K).

Resonance Raman spectra were recorded on a home-assembled UV Raman spectrograph using a Jobin-Yvon T64000 triple-stage spectrograph with spectral resolution of 2 cm^{-1}. The laser line at 325 nm of a He-Cd laser was used as an exciting source for the Raman spectroscopy. The powder X-ray diffraction (XRD) patterns were recorded on a Rigaku MiniFlex diffractometer with Cu Kα radiation source. 2θ range is 20–80° at a step size of 0.02 and a scanning speed of 5°/min. The morphology of the ZnS samples were investigated with a scanning electron microscope (SEM, FEI quanta 200F) with accelerating voltage of 0.5–30 kV and a transmission electron microscope (TEM, FEI Tecnai G2 Spirit). High-resolution transmission electron microscopy (HRTEM) measurements were also carried out using a FEI Tecnai G2 F30 transmission electron microscope.

3. Results and discussion

3.1 Structure and morphology of ZnS nanocrystals

Fig. 1 shows the X-ray diffraction patterns of ZnS samples sintered at different temperatures (873–1173 K). The three peaks at 28.52, 47.48, and 56.32° correspond to the 111, 220, and 311 planes of cubic zinc sulfide, respectively. The typical broadening of the three diffraction peaks for ZnS-P sample indicates that the size of the ZnS particles is very small. After the heat treatment processes, ZnS maintains the initial crystal structure of the sphalerite and grows to the directions of (111), (220) and (311). In the meantime, very weak diffraction peaks are observed at 26.88, 30.48 and 51.70°, indicating that there is a little fraction of ZnS in wurtzite structure. All ZnS-T samples mainly exhibit the cubic structure, since the structure transformation of pure ZnS always occurs above 1173 K.[30,37]

Fig. 2 shows TEM and SEM images of ZnS samples. The particle size of ZnS-P sample is about 3 nm. The ZnS particles grow larger and larger as the treatment temperature increasing. The diameter of ZnS particles increases from about 50 nm to about 500 nm with the treatment temperature increasing from 873 K to 1173 K. The TEM images for the ZnS-873 and ZnS-973 have stripe patterns, which are composed of alternations with light and shaded regions. TEM images become homogeneous black contrast when the treatment temperature was increased to over 1073 K. The stripe patterns for the particles smaller than 200 nm are still very distinct (Fig. 2d, inset). In addition, ZnS particles larger than 200 nm are not spherical but full of edges after being sintered at temperatures higher than 1073 K (Fig. 2i and j), further demonstrating the high crystallinity of the ZnS-T samples.

Fig. 3 displays the representative HRTEM image of ZnS nanoparticles with stripe pattern in ZnS-873. The corresponding low magnification TEM image and fast fourier transform pattern (FFT) are also shown. It should be mentioned that TEM images of ZnS particles with homogeneous contrast might indicate small quantity of defects. For the ZnS nanoparticles with stripe pattern images, stacking faults are observed between the domain A and B while twin structures are found between domain B and C. In the edge of the stacking faults or between the two twin domains (see the interfaces marked by long lines), dislocations accompany them. These results suggest that the appearance of stripe pattern in the TEM images is due to the presence of interfacial defect structures. Therefore, a large amount of defects exist in ZnS-873 and ZnS-973, while the total quantity of defects in ZnS-1073 and ZnS-1173 decreases dramatically.

Fig. 4 displays Resonance Raman spectra of ZnS excited by a 325 nm laser. The spectrum of ZnS-P sample shows Raman peaks at 276, 347, 435, 486, 568 and 697 cm^{-1} (Fig. 4c). As reported by Kumar *et al.*,[38] these Raman peaks are assigned as surface optical (SO) phonon, LO, (LO + TA), (2TO − TA), 2TO and 2LO modes of ZnS nanoparticles with size smaller than 3 nm. For the ZnS samples sintered at high temperatures, six main peaks at 347, 697, 1045, 1393, 1740, and 2090 cm^{-1} are identified as the first-order (1LO) to the sixth-order (6LO) optical phonons peaks, respectively. The appearance of the multiple Resonance Raman peaks indicates that these ZnS samples have a large value of Huang-Rhys parameter and a good optical quality.[39,40]

Electron–phonon coupling is an important issue in semiconductor materials, because it has significant influence on the optical and electrical properties of semiconductors, such as the phonon replicas of excitons and the energy relaxation rate of excited carriers in the luminescence spectra. The 2LO/1LO ratio is the parameter to specify the strength of the electron–phonon interaction.[41,42] The intensity ratios of 2LO/1LO are about 0.2, 1.2, 1.5, 2.7 and 3.2 for ZnS-P, ZnS-873, ZnS-973, ZnS-1073 and ZnS-1173 nanocrystals, respectively. The value of the ratio was found to increase with the size of ZnS nanoparticles. Although our smallest sample is still larger than the exciton radius (2.5 nm) of the ZnS bulk material,[43] we report here the correlation of the increasing electron–phonon

 This journal is © the Owner Societies 2011

View Article Online

Published on 31 January 2011. Downloaded by Dalian Institute of Chemical Physics, CAS on 9/2/2019 6:21:22 AM.

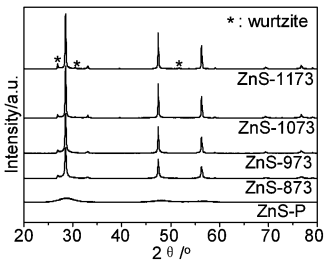

Fig. 1 XRD patterns of ZnS sintered at various temperatures. "Asterisk" denotes the wurtzite phase of ZnS.

interaction with increasing nanocrystal size. This phenomenon is observed in pure ZnS particles for the first time. The enhancement of electron–phonon coupling when increasing the nanocrystal size is mainly associated with the Fröhlich interaction. The different strength of electron–phonon coupling may induce different optical features of ZnS nanocrystals.

Four abnormal weak peaks situated at 276, 623, 975 and 1322 cm^{-1} are also observed in the Resonance Raman spectra apart from those strong higher-order LO peaks, and they are attributed to surface optical phonon scattering (Fig. 4b). The Resonance Raman scattering is highly sensitive and can detect the weak surface phonon signal.[40,44] Luo *et al.*[40] also observed the surface optical phonon scattering from hollow ZnS microspheres, and the defects on the surface of the hollow ZnS microspheres are considered as the origin of the SO modes. Therefore, the SO modes may be attributed to the surface and interfacial defects of ZnS generated during heat treatment processes.

The crystallinity of the ZnS sample increases with the heat treatment, when the structure of the ZnS maintains the cubic structure. ZnS particles grow larger through the agglomeration of particles during the heat treatment. The electron–phonon coupling increases with increasing nanocrystal size of the ZnS samples. The HRTEM results and the SO modes in Resonance Raman spectra indicate that the surface and interfacial defects are formed in ZnS during the agglomeration processes. Moreover, the point defects in ZnS crystals and that associated with stacking fault and twin structures may vary considerably for ZnS sintered at different temperatures, because the following reactions may take place during the heat treatment processes of ZnS in H_2S atmosphere:[13,23,27,29]

$$Zn(s) + H_2S(g) \rightarrow ZnS(s) + H_2(g) \quad (1)$$

$$2H_2S(g) \rightarrow S_2(s) + 2H_2(g) \quad (2)$$

$$ZnS(s) + H_2(g) \rightarrow Zn(s) + H_2S(g) \quad (3)$$

The preparation of ZnS nanostructures *via* thermal evaporation method is always based on the reactions (1) and (3).[13,23,27,29] Reaction (1) can occur automatically for it is thermodynamically favourable. But reaction (3) is a strongly endothermic reaction and might only occur at very high temperatures. Importantly, reaction (2) is also thermodynamically unfavourable. The thermal decomposition of H_2S can only occur with temperatures above 1073 K.[45,46] As a result, reactions (2) and (3) can only occur when treatment temperatures are higher than 1073 K. This is due to H_2 produced from reaction (2). Therefore, when treatment temperatures are lower than 973 K, only reaction (1) occurs. However, reactions (1) to (3) happen simultaneously when the treatment temperatures are higher than 1073 K.

Reaction (1) can eliminate the sulfur vacancies in ZnS. Interstitial sulfur atoms are formed through the decomposition of H_2S, as shown in reaction (2). And sulfur vacancies appear in ZnS because of reaction (3). As a result, ZnS-873 and ZnS-973 may contain little sulfur vacancies while interstitial sulfur and sulfur vacancies might coexist in ZnS-1073 and ZnS-1173 particles. The ZnS nanocrystals with different defect states and different strength of electron–phonon coupling may exhibit various PL characteristics.

3.2 Optical properties of ZnS nanocrystals

Fig. 5a shows emission spectra of ZnS samples at room temperature. Only a blue emission band centered at about 430 nm is clearly observed for ZnS-P sample. The blue emission can be attributed to the surface states.[47,48] ZnS-873 sample sintered at 873 K only shows the wide orange emission band

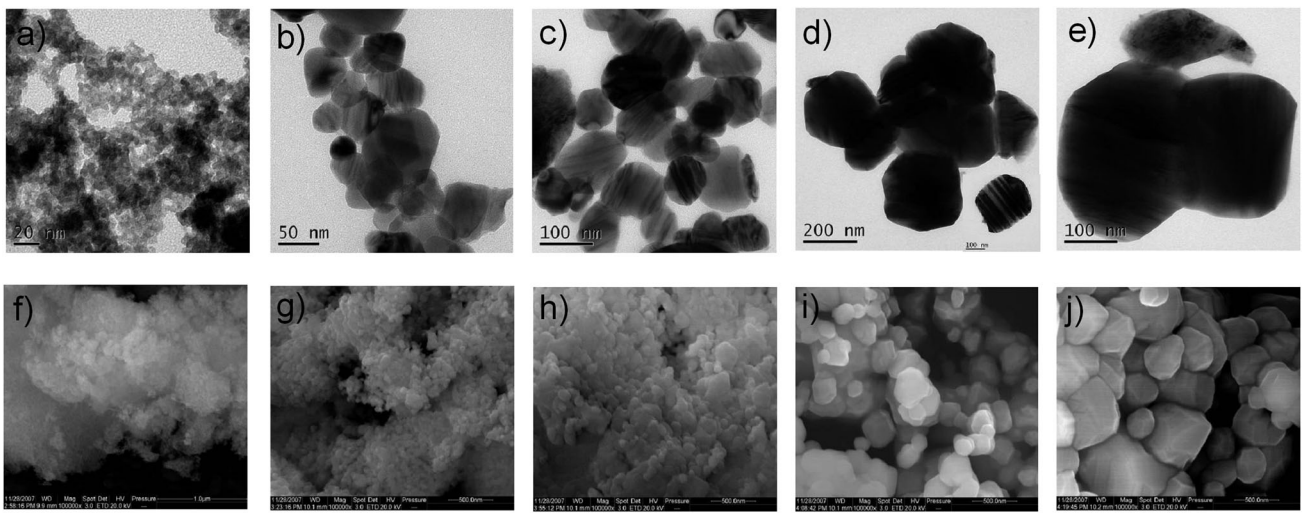

Fig. 2 TEM images of ZnS-P (a), ZnS-873 (b), ZnS-973 (c), ZnS-1073 (d), ZnS-1173 (e) and SEM images of ZnS-P (f), ZnS-873 (g), ZnS-973 (h), ZnS-1073 (i), ZnS-1173 (j) samples.

View Article Online

Published on 31 January 2011. Downloaded by Dalian Institute of Chemical Physics, CAS on 9/2/2019 6:21:22 AM.

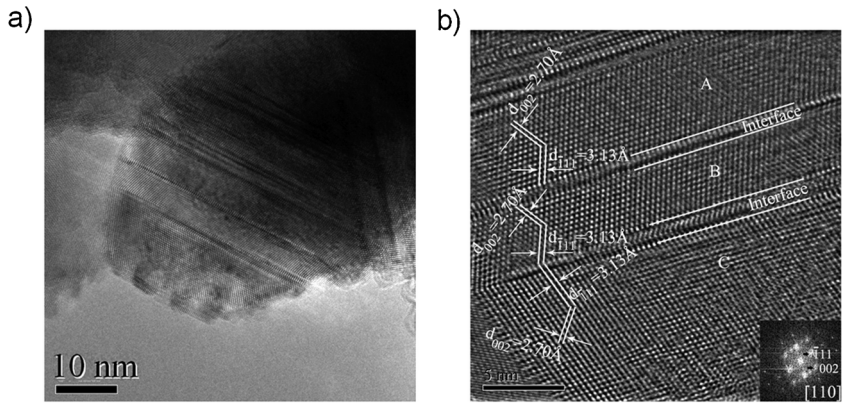

Fig. 3 TEM (a) and HRTEM (b) images of one representative nanoparticle with stripe pattern in ZnS-873. The inserted image is the corresponding fast fourier transform pattern (FFT) of domain C.

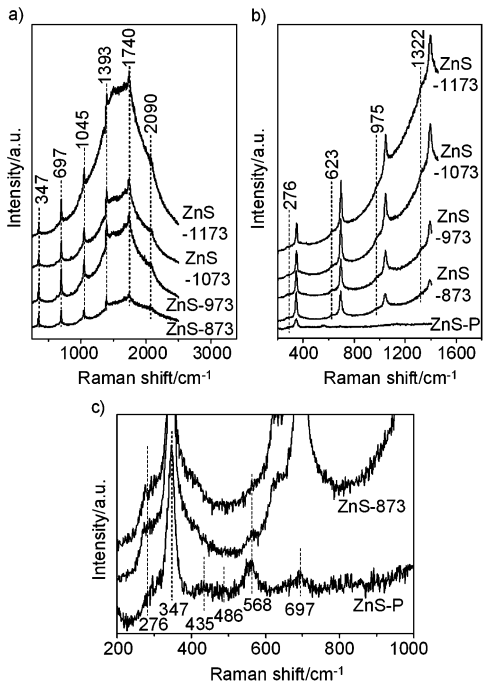

Fig. 4 Resonance Raman spectra of ZnS sintered at various temperatures.

centered at about 620 nm while the blue emission at around 430 nm disappears. The orange emission band grows stronger with the treatment temperature further increasing to 973 K. The full-width at half-maximum of the emission band in ZnS-973 increases clearly due to the widening from 500 to 600 nm, indicating that a new emission band appears in this range. Accordingly, a new green emission band centered at around 515 nm is observed when the treatment temperature was raised to 1073 K. The green emission band grows very intense and the orange emission band becomes very weak in comparison as the treatment temperature increasing to 1173 K. It should be mentioned that the emission intensity increases considerably with the treatment temperature greater than 1073 K. Therefore, various emission properties can be obtained by simply changing the treatment temperatures of ZnS samples.

Fig. 5b shows the emission spectra of ZnS films at 77 K. Similar to the results at room temperature, the ZnS-P sample displays the blue emission band at about 430 nm, and the ZnS-1073 and ZnS-1173 samples exhibit the green emission band at 515 nm and the orange emission band at 620 nm. Interestingly, the green and orange emission bands are also observed simultaneously in ZnS-873 and ZnS-973 samples. This phenomenon is distinctly different from the emission characteristics at room temperature. It reflects different measurement-temperature dependence of the green and orange emission bands in ZnS samples. This indicates the different properties of defects associated with the green and orange PL.

Fig. 6 displays the measurement-temperature dependence of PL intensities of the green and orange emission bands. It should be mentioned that the PL intensity was obtained after the measurement-temperature staying at the temperature for more than 20 min to ensure the accuracy of the measurement-temperature. In addition, the temperature accuracy can reach 0.1 K with the Oxford cryostat. The luminescence intensity for the green emission in ZnS-873 and ZnS-973 and the orange emission in all samples decreases monotonically with an increasing measured temperature. This trend is because of the increase in the nonradiative recombination probability of electrons and holes with increasing measurement-temperature. Amazingly, the measurement-temperature dependence of the green emission intensity of ZnS-1073 and ZnS-1173 samples shows the totally different behaviors (Fig. 6a). That is, the intensity of the green emission band shows a clear increase with increasing temperature in the temperature range from 150 K to 200 K. This phenomenon has been widely studied in ZnO nanocrystals in recent years,[49,50] and is referred to as negative thermal quenching (NTQ).

He *et al.*[49] demonstrate that the surface states play a very important role in the optical properties of ZnO nanostructures and the NTQ is interpreted in terms of a multiple trapping-detrapping process by surface states. Therefore, the NTQ, which is only observed for the ZnS-1073 and ZnS-1173 samples, may be due to the unique energy levels of defects in ZnS-1073 and ZnS-1173. Meanwhile, the concentration of defect states is suitable for the observation of NTQ in the ZnS-1073 and ZnS-1173 samples.

Fig. 7 shows the photoluminescence excitation spectra for the various visible emission bands at 77 K. The excitation

 This journal is © the Owner Societies 2011

View Article Online

Published on 31 January 2011. Downloaded by Dalian Institute of Chemical Physics, CAS on 9/2/2019 6:21:22 AM.

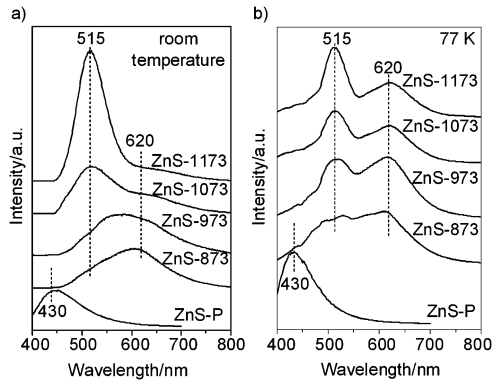

Fig. 5 Emission spectra of ZnS excited by 325 nm light at room temperature (a) and at 77 K (b).

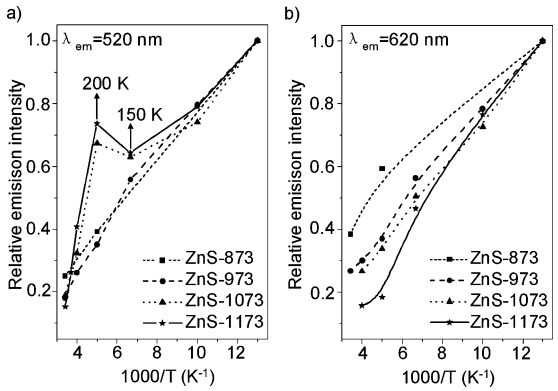

Fig. 6 Measurement-temperature dependence of emission intensity of the green (a) and orange (b) emission bands in ZnS.

features for the blue emission band in ZnS-P sample only exhibit the interband excitation band, which appears at 335 nm. But the interband excitation band of ZnS-T samples appears at 325 nm. The red shift from 325 nm to 335 nm indicates that a large amount of defect states exist near the edge of the energy band in ZnS-P and contribute to the blue emission band.

ZnS-T samples all exhibit the interband excitation band at 325 nm (Fig. 7a) when the green emission band is concerned. The excitation signal for ZnS-873 and ZnS-973 shows a rising trend from 335 nm to 430 nm, suggesting that there is a large quantity of defects contributing to the green emission. The excitation signal in the range from 335 nm to 430 nm decreases dramatically with increasing treatment temperature. When the treatment temperature reaches 1173 K, the excitation signal in the range from 335 nm to 430 nm is very weak with no rising trend (Fig. 7c), indicating that the total quantity of defects is very small. As a result, the total amount of defect states is suitable for the NTQ in ZnS-1073 and ZnS-1173 while too many defects make trapped carriers relax mainly through nonradiative processes in ZnS-873 and ZnS-973.

The excitation signal of orange emission in ZnS-873 and ZnS-973 shows a continuous increase in the range from 330 nm to 520 nm similar to the excitation features of green luminescence. The excitation signal becomes very weak in the range from 335 nm to 400 nm for ZnS-1073 and ZnS-1173 (Fig. 7c). These results further confirm that a mass of defects exist in ZnS-873 and ZnS-973 while the total quantity of defects is very small in ZnS-1073 and ZnS-1173. The large quantity of defects in ZnS-873 and ZnS-973 are assigned to the surface and interfacial defects generated in ZnS samples during treatment process.[26] However, the treatment temperatures above 1073 K make the ZnS particle get higher crystallinity. Consequently, ZnS-1073 and ZnS-1173 have much less defects than ZnS-873 and ZnS-973.

3.3 Carrier dynamics of ZnS nanocrystals

Time-resolved PL spectra were measured at 77 K to obtain more information about the origins of the various emission bands. Time-resolved PL spectra of the ZnS-1173 sample monitored at 520 nm and 630 nm are shown in Fig. 8. The excitation wavelength changes from 300 nm to 420 nm with the interval of 20 nm. The luminescence decays faster as the excitation wavelength increases when the green emission is monitored. Namely, the luminescence decay processes finish in 200 μs when the excitation wavelength is longer than 340 nm. But when the excitation light is 300 nm or 320 nm, the green emission decay processes do not finish in 400 μs.

On the other hand, the decay processes of the orange emission are different. The decay rate decreases with increasing excitation wavelength from 300 to 380 nm. Above 380 nm however, the decay rate increases with increasing excitation wavelength. Thus, the decay processes of the orange emission band finish within 200 μs with 300 nm or 420 nm light as excitation source. But it extends to 600 μs when the excitation light is in the range from 340 nm to 400 nm. These results suggest that many defect levels exist in the range from 3.10 eV (400 nm) to 3.65 eV (340 nm) above the valence band. These defect levels mainly contribute to the slow decay component of the orange emission. The similar phenomenon is also observed for the orange luminescence in ZnS-973 and ZnS-1073, though the change trend is very small for ZnS-973 sample (data not shown). However, the change of decay rates on excitation wavelength for the orange luminescence in ZnS-873 is not observed. This is most-likely because the nonradiative processes dominate the relaxation processes of the trapped carriers in ZnS-873 and ZnS-973 for the greater quantity defects.

The 325 and 355 nm are selected as the excitation lines to investigate the dynamic characteristics of the orange emission in ZnS (Fig. 9), because the carrier dynamics are sensitive to the excitation wavelength. Table 1 lists the fitted results of the decay curves with the 325 nm excitation line. All samples exhibit biexponential behavior with a fast decay in hundreds of nanosecond and a slow decay in tens of microsecond. The decay curve of ZnS-873 is well described with the fast lifetime of 0.42 μs (85.5%) and the slow lifetime of 98.49 μs (14.5%). The slow lifetime is shortened while the fast lifetime remains unchanged with the treatment temperature increasing. In the meantime, the relative content of the slow lifetime component is decreasing. Consequently, the lifetimes for ZnS-1173 are 0.39 μs (96.3%) and 46.49 μs (3.7%).

Fig. 9b displays the decay profiles of the orange emission excited by 355 nm. The corresponding fit results are displayed in Table 2. A fast lifetime of 0.27 μs (87.5%) and a slow one of 83.65 μs (12.5%) are obtained in ZnS-873. In accord with the results excited by 325 nm, the slow lifetime becomes fast while

View Article Online

Published on 31 January 2011. Downloaded by Dalian Institute of Chemical Physics, CAS on 9/2/2019 6:21:22 AM.

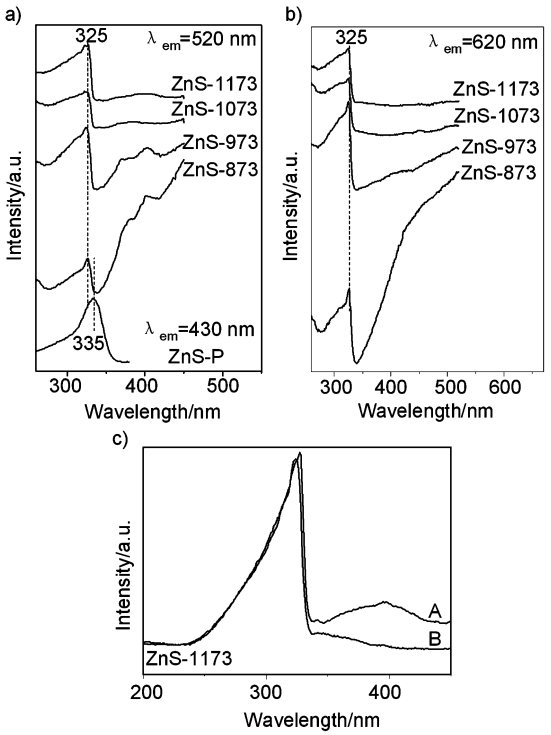

Fig. 7 Excitation spectra of ZnS-P monitored at 430 nm and ZnS-T samples monitored at 520 nm (a) and 620 nm (b) at 77 K. (c) Excitation spectra of ZnS-1173 sample with the monitored wavelength at 520 nm (A) and 620 nm (B).

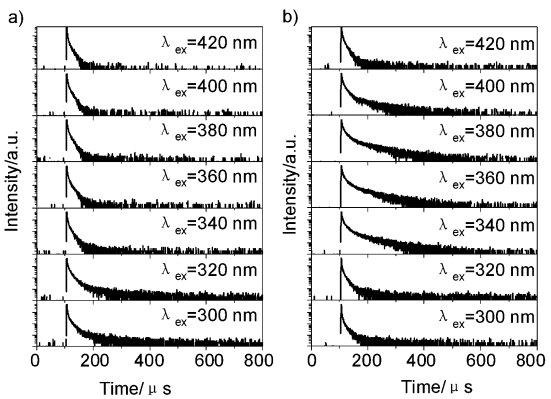

Fig. 8 Time-resolved photoluminescence spectra monitored at 520 nm (a) and 630 nm (b) for ZnS-1173 sample at 77 K.

the fast lifetime remains relatively unchanged with the treatment temperature increasing. But the relative content of the slow lifetime increases with increasing treatment temperature. This trend is opposite to that of the orange emission excited by 325 nm. As a result, the relative content of slow lifetime reaches to 46.8% when the treatment temperature is 1173 K.

The fast and slow decay of orange luminescence are attributed to two different relaxation processes. The fast decay is assigned to the direct recombination of electrons and holes at luminescent sites. Thus, it is nearly not changed with increasing treatment temperature. The slow decay is due to the trapped electrons, which is captured by shallow defect states first and then relax to the luminescent sites. The total quantity of defect

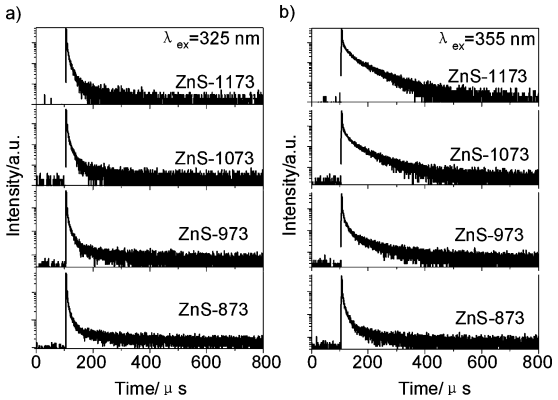

Fig. 9 Time-resolved photoluminescence spectra of ZnS with the excitation light at 325 nm (a) and 355 nm (b) at 77 K. The monitored emission wavelength is 630 nm.

Table 1 Fit results of PL decay curves of ZnS treated at various temperatures with the monitored wavelength at 630 nm excited by 325 nm light at 77 K

λ_{ex} = 325 nm	τ_1/μs	τ_2/μs	χ^2
ZnS-873	0.42 (85.5%)	98.49 (14.5%)	1.181
ZnS-973	0.39 (89.6%)	95.70 (10.4%)	1.395
ZnS-1073	0.39 (95.4%)	50.34 (4.6%)	1.121
ZnS-1173	0.39 (96.3%)	46.49 (3.7%)	1.098

states decreases dramatically as the treatment temperature increases. The decrease in defect states makes the relaxation processes through shallow defect states accelerate. As a result, the slow lifetime of orange emission is shortened with increasing treatment temperature.

The excited electrons and holes are generated in conduction and valence bands of ZnS, respectively, when the excitation light is 325 nm. The recombination processes through shallow defect states are decreased with the treatment temperature increasing, since the amount of shallow defect states is reduced. Thus, the relative content of the slow lifetime relaxation process decreases at higher treatment temperatures. On the other hand, the trapped electrons are generated directly near the luminescent sites when 355 nm light is used as excitation source. More defect states make more trapped electrons relax nonradiatively. Consequently, less defect states in ZnS obtained at higher treatment temperature mean that more trapped electrons can contribute to the orange emission. As a result, the relative content of slow lifetime process increases with increasing treatment temperature.

The time-resolved emission spectra of ZnS-1173 are studied with 355 nm light as excitation source to further understand the luminescence properties of ZnS, as plotted in Fig. 10. The decay rates are very sensitive to the monitored wavelength. When the detection wavelength is 480 nm, the decay rates are nearly as fast as that of the instrumental response. It becomes slower with an increase in monitored wavelength. Such a behavior suggests that both the green and orange luminescence are caused by donor–acceptor recombination.[51,52] The fit results for these decay profiles are listed in Table 3. With the detection wavelength increasing from 560 nm to 680 nm, the fast lifetime is almost unchanged while the slow lifetime

 This journal is © the Owner Societies 2011

View Article Online

Published on 31 January 2011. Downloaded by Dalian Institute of Chemical Physics, CAS on 9/2/2019 6:21:22 AM.

Table 2 Time-resolved PL decay time constants of ZnS sintered at various temperatures monitored at 630 nm when 355 nm is used as excitation source at 77 K

λ_{ex} = 355 nm	τ_1/μs	τ_2/μs	χ^2
ZnS-873	0.27 (87.5%)	83.65 (12.5%)	1.263
ZnS-973	0.42 (77.9%)	77.53 (22.1%)	1.374
ZnS-1073	0.45 (64.7%)	60.87 (35.3%)	1.420
ZnS-1173	0.47 (53.2%)	55.18 (46.8%)	1.130

increases from 37.80 μs to 82.02 μs. Correspondingly, the relative content of the slow lifetime increases from 23.0% to 54.4%. It is clearly demonstrated that the orange PL is caused by the donor–acceptor recombination.

3.4 Origins of visible emissions from ZnS nanocrystals

ZnS-P is obtained by precipitation method without any post treatment. Therefore, a number of surface states with various properties exist for the small size and low crystallinity of ZnS-P particles. This is the reason for the assignment of surface states as the origin of the blue PL in ZnS-P. The ZnS-T samples are prepared from ZnS-P through heat treatment at high temperatures in H_2S atmosphere. The treatment processes can largely alter the crystallinity and the properties of the defect states, including the energy levels and the quantity of defect states. Consequently, ZnS-873 and ZnS-973 have a large amount of surface and interfacial defect states while the total number of defects in ZnS-1073 and ZnS-1173 is reduced dramatically due to the high crystallinity. In addition, the enhancement of electron–phonon coupling in ZnS-1073 and ZnS-1173 may also influence their emission properties.

The dislocation-induced photoluminescence is displayed as narrow lines in the PL spectra, while excitons are localized on the stacking faults.[53,54] Therefore, the broad defect emissions in ZnS in this study may be related to the point defects, which always serve as luminescent sites during photoluminescence processes. Importantly, four types of point defects can present in pure ZnS particles (Fig. 11a).[55,56] They are sulfur vacancies, zinc vacancies, interstitial zinc atoms and interstitial sulfur atoms. As mentioned above, the reactions (1) to (3) exhibit different reactivity at different temperatures. Therefore, ZnS-873 and ZnS-973 contain little sulfur vacancies, while interstitial sulfur and sulfur vacancies may coexist in ZnS-1073 and ZnS-1173 though the total quantity of defects is very small. As a result, the zinc vacancies and interstitial zinc atoms dominate the point defects in ZnS-873 and ZnS-973, and the point defects are mainly the sulfur vacancies and interstitial sulfur atoms for ZnS-1073 and ZnS-1173.

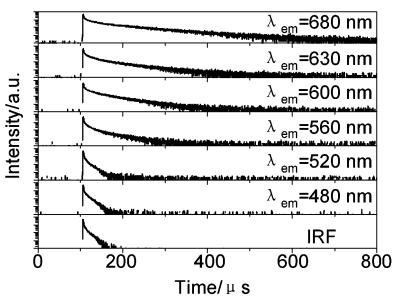

Fig. 10 Time-resolved emission spectra of the ZnS-1173 sample at 77 K. The excitation light is 355 nm.

The schematic energy level diagram with the four types of point defects is plotted in Fig. 11b. Sulfur vacancies and interstitial zinc atoms are equivalent localized donor states, while zinc vacancies and interstitial sulfur atoms lead to acceptor states.[57] Denzler *et al.*[55] reported that interstitial sulfur states should be located closer to the valence band edge than interstitial zinc states to the conduction band edge while sulfur vacancies should be located closer to the conduction band edge than zinc vacancies to the valence band edge. Moreover, energy levels of vacancies are deeper than interstitial states.

In combination with the results of PLE and time-resolved results, the excitation and emission features of ZnS are proposed in Fig. 11b. Electrons can be excited to the sulfur vacancies with the excitation energy higher than 2.88 eV (430 nm), which is equivalent to the excitation edge for green luminescence. It is reported that the green PL is related to elemental sulfur species in ZnS.[20,35] Thus, the transfer of trapped electrons on sulfur vacancies to interstitial sulfur states produces the green luminescence. At the same time, excitation light with energy higher than 3.10 eV (400 nm), evidenced by PLE and time-resolved PL results, can excite the electrons to states of interstitial zinc. The zinc vacancies, which exist at about 1.1 eV above the valence band in ZnS,[31,32] serve as the acceptor levels for the photoinduced holes. The orange emission is assigned to the recombination between the interstitial zinc states and the zinc vacancies.

The assignments of green and orange emission are also supported by the time-resolved PL results. Because the interstitial sulfur atoms and sulfur vacancies in ZnS-1073 and ZnS-1173 are mainly formed by reactions (2) and (3), the distance between sulfur vacancies and interstitial sulfur atoms is always very short. On the contrary, the distribution of the zinc vacancies and interstitial zinc atoms is random. Consequently, the zinc vacancies are always far away from the interstitial zinc atoms. Thus, the radiation recombination probability to produce the green emission is much higher than that to produce the orange luminescence. That may be the reason that the green emission intensity in ZnS-1173 is much higher than the orange emission intensity in ZnS-873. More importantly, the long distance makes the recombination rate between zinc vacancies and interstitial zinc atoms slow. As a result, the lifetimes of orange emission are much longer than that of the green luminescence, and the carrier dynamics of orange emission are very sensitive to the change of the defect properties in ZnS.

4. Conclusions

ZnS nanocrystals with various visible emission properties were investigated. The electron–phonon coupling in ZnS increases with the size increasing. The enhancement of electron–phonon coupling affects the optical properties of ZnS. The blue (430 nm), green (515 nm) and orange (620 nm) luminescence are exhibited for these ZnS nanocrystals due to the different defect properties. The blue emission is attributed to surface states of ZnS without any treatment, while the green and orange emission bands are assigned to the electron transfer from sulfur vacancies to interstitial sulfur states and the recombination between

View Article Online

Published on 31 January 2011. Downloaded by Dalian Institute of Chemical Physics, CAS on 9/2/2019 6:21:22 AM.

Table 3 Time-resolved PL decay time constants of ZnS treated at 1173 K with 355 nm excitation light at 77 K

λ_{em}	τ_1/μs	τ_2/μs	χ^2
560 nm	0.46 (77.9%)	37.80 (23.0%)	1.061
600 nm	0.46 (54.8%)	44.99 (45.2%)	1.075
630 nm	0.47 (53.2%)	55.17 (46.8%)	1.131
680 nm	0.48 (45.6%)	82.02 (54.4%)	1.605

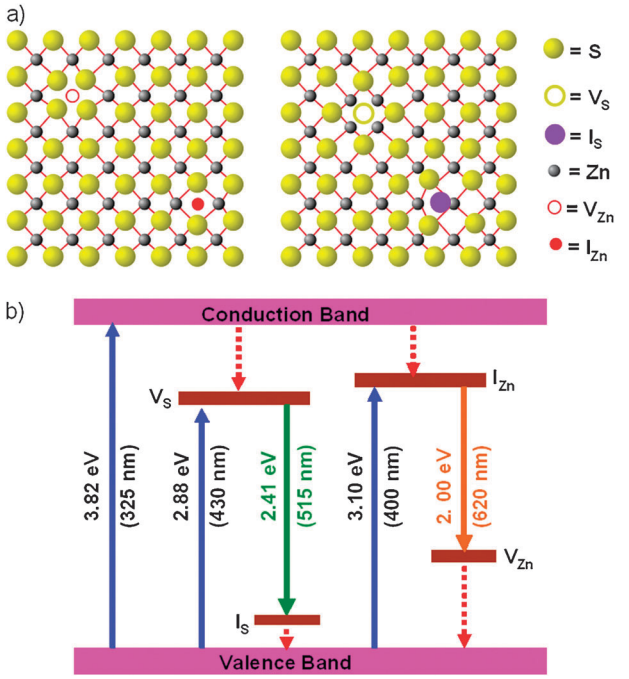

Fig. 11 (a) Schematics of point defects that may occur in pure ZnS. (b) Schematic energy level diagram for the point defects in ZnS: I_s = interstitial sulfur, I_{Zn} = interstitial zinc, V_s = sulfur vacancy, and V_{Zn} = zinc vacancy. The levels are drawn corresponding to the peaks in the PL and PLE spectra of ZnS.

interstitial zinc states and zinc vacancies, respectively. The orange emission exhibits slower relaxation processes than the green luminescence because of the longer distance between luminescent sites. In summary, various visible emission characteristics were obtained in ZnS nanocrystals by changing the properties of defects in ZnS. Therefore, it is indispensable to design and control defect states to tune the ZnS properties for the application in light emitting displays, optoelectronic devices, *etc.*

Acknowledgements

The authors are grateful to the National Basic Research Program of China (2009CB220010), National Natural Science Foundation of China (20903093) and Programme for Strategic Scientific Alliances between China and the Netherlands (2008DFB50130) for financial support.

Notes and references

1 X. S. Fang, Y. Bando, G. Z. Shen, C. H. Ye, U. K. Gautam, P. M. F. J. Costa, C. Y. Zhi, C. C. Tang and D. Golberg, *Adv. Mater.*, 2007, **19**, 2593–2596.
2 X. S. Fang, Y. Bando, C. H. Ye, G. Z. Shen and D. Golberg, *J. Phys. Chem. C*, 2007, **111**, 8469–8474.
3 X. S. Fang, Y. Bando, M. Y. Liao, U. K. Gautam, C. Y. Zhi, B. Dierre, B. D. Liu, T. Y. Zhai, T. Sekiguchi, Y. Koide and D. Golberg, *Adv. Mater.*, 2009, **21**, 2034–2039.
4 D. Q. Chen, Y. L. Yu, P. Huang, H. Lin, Z. F. Shan, L. W. Zeng, A. P. Yang and Y. S. Wang, *Phys. Chem. Chem. Phys.*, 2010, **12**, 7775–7778.
5 T. Torimoto, T. Adachi, K. Okazaki, M. Sakuraoka, T. Shibayama, B. Ohtani, A. Kudo and S. Kuwabata, *J. Am. Chem. Soc.*, 2007, **129**, 12388–12389.
6 S. L. Xiong, B. J. Xi, C. M. Wang, D. C. Xu, X. M. Feng, Z. C. Zhu and Y. T. Qian, *Adv. Funct. Mater.*, 2007, **17**, 2728–2738.
7 C. Feigl, S. P. Russo and A. S. Barnard, *J. Mater. Chem.*, 2010, **20**, 4971–4980.
8 K. Manzoor, S. R. Vadera, N. Kumar and T. R. N. Kutty, *Appl. Phys. Lett.*, 2004, **84**, 284–286.
9 H. Hu and W. Zhang, *Opt. Mater.*, 2006, **28**, 536–550.
10 M. R. Kim, J. H. Chung and D. J. Jang, *Phys. Chem. Chem. Phys.*, 2009, **11**, 1003–1006.
11 A. A. Bol and A. Meijerink, *Phys. Chem. Chem. Phys.*, 2001, **3**, 2105–2112.
12 F. H. Su, Z. L. Fang, B. S. Ma, K. Ding, G. H. Li and S. J. Xu, *J. Appl. Phys.*, 2004, **95**, 3344–3349.
13 X. S. Fang, T. Y. Zhai, U. K. Gautam, L. Li, L. M. Wu, Y. Bando and D. Golberg, *Prog. Mater. Sci.*, 2011, **56**, 175–287.
14 Y. Y. Tay, T. T. Tan, F. Boey, M. H. Liang, J. Ye, Y. Zhao, T. Norby and S. Li, *Phys. Chem. Chem. Phys.*, 2010, **12**, 2373–2379.
15 S. Kar and S. Chaudhuri, *J. Phys. Chem. B*, 2005, **109**, 3298–3302.
16 P. A. Hu, Y. Q. Liu, L. C. Cao and D. B. Zhu, *J. Phys. Chem. B*, 2004, **108**, 936–938.
17 Z. X. Zhang, J. X. Wang, H. J. Yuan, Y. Gao, D. F. Liu, L. Song, Y. J. Xiang, X. W. Zhao, L. F. Liu, S. D. Luo, X. Y. Dou, S. C. Mou, W. Y. Zhou and S. S. Xie, *J. Phys. Chem. B*, 2005, **109**, 18352–18355.
18 X. S. Fang, U. K. Gautam, Y. Bando, B. Dierre, T. Sekiguchi and D. Golberg, *J. Phys. Chem. C*, 2008, **112**, 4735–4742.
19 J. F. Gong, S. G. Yang, J. H. Duan, R. Zhang and Y. W. Du, *Chem. Commun.*, 2005, 351–353.
20 C. H. Ye, X. S. Fang, G. H. Li and L. D. Zhang, *Appl. Phys. Lett.*, 2004, **85**, 3035–3037.
21 X. S. Fang, C. H. Ye, L. D. Zhang, Y. H. Wang and Y. C. Wu, *Adv. Funct. Mater.*, 2005, **15**, 63–68.
22 J. Q. Hu, Y. Bando, J. H. Zhan and D. Golberg, *Angew. Chem., Int. Ed.*, 2004, **43**, 4606–4609.
23 Y. Jiang, X. M. Meng, J. Liu, Z. Y. Xie, C. S. Lee and S. T. Lee, *Adv. Mater.*, 2003, **15**, 323–327.
24 L. Shi, K. Y. Bao, J. Cao and Y. T. Qian, *CrystEngComm*, 2009, **11**, 2308–2312.
25 G. Z. Shen, Y. Bando, C. C. Tang and D. Golberg, *J. Phys. Chem. B*, 2006, **110**, 7199–7202.
26 Y. G. Zhang, F. Lu, Z. Y. Wang, H. X. Wang, M. G. Kong, X. G. Zhu and L. D. Zhang, *Cryst. Growth Des.*, 2007, **7**, 1459–1462.
27 Z. Y. He, Y. Su, Y. Q. Chen, D. Cai, J. Jiang and L. Chen, *Mater. Res. Bull.*, 2005, **40**, 1308–1313.
28 Y. Arao, Y. Hirooka, K. Tsuchiya and Y. Mori, *J. Phys. Chem. C*, 2009, **113**, 894–899.
29 X. H. Zhang, Y. Zhang, Y. P. Song, Z. Wang and D. P. Yu, *Physica. E*, 2005, **28**, 1–6.
30 J. C. Lee and D. H. Park, *Mater. Lett.*, 2003, **57**, 2872–2878.
31 M. Salavati-Niasari, M. R. Loghman-Estarki and F. Davar, *J. Alloys Compd.*, 2009, **475**, 782–788.
32 X. J. Wang, F. Q. Wan, K. Han, C. X. Chai and K. Jiang, *Mater. Charact.*, 2008, **59**, 1765–1770.
33 H. Zhang, S. Y. Zhang, M. Zuo, G. P. Li and J. G. Hou, *Eur. J. Inorg. Chem.*, 2005, 47–50.
34 S. Kar and S. Chaudhuri, *Chem. Phys. Lett.*, 2005, **414**, 40–46.
35 C. H. Ye, X. S. Fang, M. Wang and L. D. Zhang, *J. Appl. Phys.*, 2006, **99**, 063504.
36 Y. C. Zhu, Y. Bando and D. F. Xue, *Appl. Phys. Lett.*, 2003, **82**, 1769–1771.
37 H. Y. Lu and S. Y. Chu, *J. Cryst. Growth*, 2004, **265**, 476–481.

 This journal is © the Owner Societies 2011

View Article Online

Published on 31 January 2011. Downloaded by Dalian Institute of Chemical Physics, CAS on 9/2/2019 6:21:22 AM.

38 S. S. Kumar, M. A. Khadar, K. G. M. Nair, S. Dhara and P. Magudapathy, *J. Raman Spectrosc.*, 2008, **39**, 1900–1906.
39 B. Kumar, H. Gong, S. Y. Chow, S. Tripathy and Y. Hua, *Appl. Phys. Lett.*, 2006, **89**, 071922.
40 Y. Y. Luo, G. T. Duan and G. H. Li, *Appl. Phys. Lett.*, 2007, **90**, 201911.
41 R. P. Wang, G. Xu and P. Jin, *Phys. Rev. B*, 2004, **69**, 113303.
42 H. M. Cheng, K. F. Lin, H. C. Hsu and W. F. Hsieh, *Appl. Phys. Lett.*, 2006, **88**, 261909.
43 B. Urbaszek, C. M. Townsley, X. Tang, C. Morhain, A. Balocchi, K. A. Prior, R. J. Nicholas and B. C. Cavenett, *Phys. Status Solidi B*, 2002, **229**, 549–552.
44 Y. M. Yu, M. H. Hyun, S. Nam, D. Lee, B. S. O, K. S. Lee, P. Y. Yu and Y. D. Choi, *J. Appl. Phys.*, 2002, **91**, 9429–9431.
45 K. Karan, A. K. Mehrotra and L. A. Behie, *AIChE J.*, 1999, **45**, 383–389.
46 M. Binoist, B. Labegorre, F. Monnet, P. D. Clark, N. I. Dowling, M. Huang, D. Archambault, E. Plasari and P. M. Marquaire, *Ind. Eng. Chem. Res.*, 2003, **42**, 3943–3951.
47 K. Sooklal, B. S. Cullum, S. M. Angel and C. J. Murphy, *J. Phys. Chem.*, 1996, **100**, 4551–4555.
48 S. Biswas, S. Kar and S. Chaudhuri, *J. Phys. Chem. B*, 2005, **109**, 17526–17530.
49 H. P. He, Z. Z. Ye, S. S. Lin, B. H. Zhao, J. Y. Huang and H. P. Tang, *J. Phys. Chem. C*, 2008, **112**, 14262–14265.
50 M. Hauser, A. Hepting, R. Hauschild, H. Zhou, J. Fallert, H. Kalt and C. Klingshirn, *Appl. Phys. Lett.*, 2008, **92**, 211105.
51 M. Oneil, J. Marohn and G. McLendon, *J. Phys. Chem.*, 1990, **94**, 4356–4363.
52 S. A. Studenikin and M. Cocivera, *J. Appl. Phys.*, 2002, **91**, 5060–5065.
53 S. A. Shevchenko and A. N. Tereshchenko, *Physica. B*, 2009, **404**, 4540–4542.
54 P. Corfdir, P. Lefebvre, J. Levrat, A. Dussaigne, J. D. Ganiere, D. Martin, J. Ristic, T. Zhu, N. Grandjean and B. Deveaud-Pledran, *J. Appl. Phys.*, 2009, **105**, 043102.
55 D. Denzler, M. Olschewski and K. Sattler, *J. Appl. Phys.*, 1998, **84**, 2841–2845.
56 A. Murugadoss and A. Chattopadhyay, *Bull. Mater. Sci.*, 2008, **31**, 533–539.
57 W. G. Becker and A. J. Bard, *J. Phys. Chem.*, 1983, **87**, 4888–4893.